



# Nonlinear inverse scattering methods for thermal wave slice tomography: A wavelet domain approach

Eric L. Miller

*Dept. of Electrical and Computer Engineering, Northeastern University,*

*235 Forsyth Building*

*Boston MA, 02115, USA*

*Tel: (617) 373-8386 Fax: (617) 373-8627*

*e-mail: elmiller@ece.neu.edu*

Lena Nicolaides and Andreas Mandelis

*Photothermal and Optoelectronic Diagnostics Laboratory*

*Dept. of Mechanical Engineering, Univ. of Toronto*

*5 King's College Road, Toronto M5S 3G8, CANADA*

*Phone/Fax: (416) 978-5106*

*e-mail: mandelis@mie.utoronto.ca*

## Abstract

A wavelet domain, non-linear inverse scattering approach is presented for imaging sub-surface defects in a material sample given observations of scattered thermal waves. Unlike methods using the Born linearization, our inversion scheme is based on the full wavefield model describing the propagation of thermal waves. Multiresolution techniques are employed to regularize and to lower the computational burden of this ill-posed imaging problem. We use newly developed wavelet-based regularization methods to resolve better the edge structures of defects relative to reconstructions obtained with smoothness-type regularizers. A non-linear approximation to the exact forward scattering model is introduced to simplify the inversion with little loss

in accuracy. We demonstrate this approach on cross-section imaging problems using synthetically generated scattering data from transmission and backprojection geometries.

## 1. Introduction

Thermal wave slice tomography (TWST) has evolved in recent years as a useful tool for non-invasively imaging and detecting defects in the bulk properties of a material sample<sup>1-3</sup>. This non-destructive evaluation (NDE) technique makes use of a modulated laser source illuminating an external surface of the material under test to induce internal thermal waves. Interaction of the thermal wave field with material inhomogeneities gives rise to scattered fields which propagate and are ultimately measured at the surface of the material. The problem of interest in this paper is, given knowledge of the applied thermal wave field and the observed scattered fields, to produce a reconstruction of the internal structure which reproduces as faithfully as possible features of interest such as defects.

The techniques we use to solve this inverse problem are based on the results of Mandelis who has shown that the thermal wavefield obeys a scalar Helmholtz equation with a complex valued, space varying propagation constant<sup>4,5</sup>. The spatial structure of this constant is related to the thermal diffusivity of the material. Because defects are reflected in changes in the thermal diffusivity, a reconstruction of the propagation constant, or a normalized form known as the object function<sup>1</sup>, yields quantitative information about the material's bulk structure.

Mathematically, the TWST inverse problem is equivalent to an inverse electrical conductivity problem which has been studied extensively in the geophysical and electromagnetics literature<sup>6-8</sup>. These ill-posed inverse problems possess a collection of interesting and well established difficulties not the least of which is that a complicated, non-linear relationship exists between the observed scattered fields and the object function. The first efforts in employing the forward scattering model of Ref. [ 4, 5] for TWST inversion have been to consider

a linearized form of the exact physics obtained under the first Born approximation<sup>1-3,9</sup>. This model takes into account diffractive effects and is most accurate when the thermal diffusivity perturbation is “small” both in size and amplitude relative to a known background<sup>10</sup>. The initial inversion results using the Born model have been quite encouraging in that images containing quantitatively useful information concerning the spatial location and magnitude of defects have been reconstructed using both simulated and experimental data<sup>1-3,9</sup>.

Here we extend the use of wavefield inversion methods for the TWST problem in a number of ways. First, a full, non-linear inverse scattering approach is used to generate the reconstruction. The resulting inversion method is iterative in nature and may allow for the more accurate reconstruction of defects whose structure falls outside of the bounds where the Born approximation is valid. We also make extensive use of wavelet methods in the formulation and the solution of the problem. Our motivation for employing these mathematical techniques is based on our previous work in wavelet-based non-linear inverse scattering<sup>11</sup>. First, the wavelet transform is known to make sparse the matrix representations of many integral operators including those arising in the TWST scattering problem<sup>12</sup>. Thus, a transform domain formulation can build on this sparsity to reduce the computational burden of generating a reconstruction. Additionally, the TWST inverse problem is highly ill-posed in the sense discussed in Ref. [13]. That is, small perturbations in the data, as would come from noise, can result in reconstructions with high amplitude, oscillatory structure. Roughly speaking, these non-physical artifacts arise because the forward scattering process is highly smoothing so that the data contain very little useful information about the high frequency structure of the object function. Attempting to extract such information without some stabilization (also known as regularization) results in distorted reconstructions.

Our previous work has demonstrated that wavelet methods can be employed in two respects for regularizing these inverse problems<sup>11,14</sup>. First, it was shown that traditional Tikhonov-type smoothness regularization schemes<sup>15</sup> could be implemented quite easily in a wavelet transform formulation. Second, by exploiting the structure of the wavelet regularizer we developed an adaptive method for determining those elements in the wavelet transform

of the object function for which the data did and did not provide useful information at each stage of the inversion. This work provided insight into the manner in which the physics of the problem along with factors such as source-receiver configuration, noise level, and prior information determined the finest scale as a function of space which could “reasonably” be obtained in the reconstruction. Additionally, we used this decomposition to reduce further the complexity of solving the inverse scattering problem.

Here, we build on these results in a number of ways. First, we introduce and demonstrate the utility of a class of wavelet regularization schemes which are appropriate for the reconstruction of objects (defects) with sharply defined boundaries. Tikhonov type regularizers typically are designed to produce smooth, low-pass reconstructions which blur important features such as edges in the image<sup>13</sup>. By making use of certain mathematical results which state that wavelets can be used as bases for a wide range of function spaces including spaces containing “edgy” objects<sup>16</sup>, we develop a new scale-space regularization method which produces significantly sharper reconstructions.

Additionally, we develop a wavelet-based, reduced complexity approximation to the forward TWST problem. As discussed in Section 4, at each stage of the iterative solution method we must compute explicitly the inverse of a large, dense matrix, a computationally intensive task. This matrix is related to the solution of the thermal-wave forward scattering problem for an object function equal to the reconstruction obtained at the previous iteration plus a small correction. By linearizing the expression for this matrix about this correction, we obtain a recursive formula in which the inverse matrix at the current iteration is equal to the one from the last iteration plus an increment due to the change in the material properties. Construction of this increment requires only the multiplication of three sparse matrices rather than the inversion of a single, large, dense matrix.

The remainder of this paper is organized as follows. In Section 2 the mathematical model underlying the TWST problem is defined. Section 3 is devoted to an overview of the wavelet transform and its application to the thermal-wave tomographic inverse. The non-linear inverse scattering algorithm is developed in Section 4 with examples of its application

to synthetic problems provided in Section 5. Finally, in Section 6, conclusions and future work are discussed.

## 2. Physical Model for TWST

As illustrated in Fig. 1, we consider TWST problems in which a modulated laser illuminates a point at the top of the material sample inducing thermal waves in the bulk. Upon scattering from inhomogeneities, whose spatial structure is defined by the real-valued object function  $g(\mathbf{r})$ , the fields are measured along an array of points either at the top (backpropagation geometry) or the bottom (transmission mode). The inversion routines are based on  $K$  such scattering experiments. The data for the  $i$ th experiment form the vector of in-phase and quadrature components of the scattered thermal-wave field measurements obtained along one of the arrays due to illumination by the laser at a given point on the top surface. One such data point for the  $i$ th experiment at location  $\mathbf{r}_k$ , denoted  $y_i(\mathbf{r}_k)$ , is

$$y_i(\mathbf{r}_k) = \int_A G(\mathbf{r}_k, \mathbf{r}') T_i(\mathbf{r}') g(\mathbf{r}') d\mathbf{r}' + n_i(\mathbf{r}_k) \quad (1)$$

where the integral on the right hand side of (1) is the scattered field and  $n_i(\mathbf{r}_k)$  is taken to be additive measurement noise. Region  $A$  is the area of space in which the defects might be found. The quantity  $G(\mathbf{r}, \mathbf{r}')$  is Green's function associated with the pseudowave Helmholtz equation for a homogeneous medium characterized by a complex propagation constant which is infinite in two dimensions and bounded by two planes in the third<sup>4,5</sup>. Finally,  $T_i(\mathbf{r})$  is the thermal wavefield internal to  $A$  which satisfies<sup>4,5</sup>

$$T_i(\mathbf{r}) = \bar{T}_i(\mathbf{r}) + \int_A G(\mathbf{r}, \mathbf{r}') T_i(\mathbf{r}') g(\mathbf{r}') d\mathbf{r}' \quad (2)$$

where  $\bar{T}_i(\mathbf{r})$  is the time-harmonic, incident thermal wavefield generated by the laser source at a given point on the top surface. The detailed expressions for  $G(\mathbf{r}, \mathbf{r}')$  and  $\bar{T}_i(\mathbf{r})$  for the planar geometry of interest here may be found elsewhere<sup>1-5</sup>.

Our algorithms are based on discrete representations of the integral equations (1) and (2) obtained using the method of moments<sup>17</sup> with a pulse-basis and Dirac testing functions.

That is, region  $A$  is pixelated into an  $N_y \times N_x$  array of rectangular pixels and the fields and object function are expanded in a series of flat top functions (i.e. zeroth order splines) indicating that these quantities are constant over small pixels in region  $A$ . After these expansions are placed into (1) and (2) and integration is performed with respect to  $\mathbf{r}'$ , the variable  $\mathbf{r}$  is discretized in (2) by requiring equality of the left and right hand sides for all points,  $\mathbf{r}_j$ , located at the center of each pixel. Upon performing this discretization process, (1) and (2) become

$$\mathbf{y}_i = \mathbf{L}_i \mathcal{D}(\mathbf{T}_i) \mathbf{g} + \mathbf{n}_i \quad (3)$$

$$\mathbf{T}_i = \bar{\mathbf{T}}_i + \mathbf{G} \mathcal{D}(\mathbf{g}) \mathbf{T}_i. \quad (4)$$

In (3),  $\mathbf{y}_i$  is the vector of observations along the array for the  $i$ th experiment. If we regard  $g(\mathbf{r})$  as an  $N_y \times N_x$  pixelated image with the pixel value at row  $m$  and column  $n$  given by the flat-top expansion coefficient  $g_{m,n}$ , then  $[\mathbf{g}]_i$ , the  $i$ th component of the vector  $\mathbf{g}$ , is related to the pixel values via the index mapping  $i = N_x(n - 1) + m$  for  $n = 1, 2, \dots, N_x$  and  $m = 1, 2, \dots, N_y$ . A similar construction holds for the internal field vector  $\mathbf{T}_i$ . In (4)  $\bar{\mathbf{T}}_i$  is the background field vector obtained from point-matching,  $\mathcal{D}(\mathbf{x})$  is a diagonal matrix whose entries are the elements of the vector  $\mathbf{x}$ , and  $\mathbf{L}_i$  and  $\mathbf{G}$  are the matrices obtained by discretizing the integral kernels in (1) and (2).  $\mathbf{n}_i$  are taken to be mutually uncorrelated, zero mean, white Gaussian noise vectors. By solving for  $\mathbf{T}_i$  in (4), and substituting the result into (3), the data are related to the object function via the non-linear model

$$\mathbf{y}_i = \mathbf{h}_i(\mathbf{g}) + \mathbf{n}_i \quad (5)$$

$$\mathbf{h}_i(\mathbf{g}) = \mathbf{L}_i \mathcal{D}[(\mathbf{I} - \mathbf{G} \mathcal{D}(\mathbf{g}))^{-1} \bar{\mathbf{T}}_i] \mathbf{g}. \quad (6)$$

The TWST problem may now be stated as follows: given data from  $K$  scattering experiments defined by the physical model in (5), determine  $\mathbf{g}$ , the vector of expansion coefficients characterizing the object function.

There are two primary difficulties in recovering  $\mathbf{g}$  from  $\mathbf{y}_i$ . The first challenge is caused by the physics of thermal-wave propagation. The strongly lossy nature of the Helmholtz

pseudowave equation underlying (5) causes  $\mathbf{h}_i$  to act essentially as a spatial low-pass filter when applied to  $\mathbf{g}$ . The data contain predominantly coarse scale averages (i.e. low frequency) information about  $\mathbf{g}$ . Finer scale information is available primarily in the areas close to the source and receiver locations where Green’s functions are singular<sup>4,5,11</sup>. Thus, attempts to reconstruct a uniform, fine scale pixelated version of the object function are prone to instabilities resulting in images which are typically characterized by non-physical, oscillatory artifacts. As described more fully in Ref. [13], for linear inverse problems where  $\mathbf{h}(\mathbf{g}) = \mathbf{H}\mathbf{g}$  for a matrix  $\mathbf{H}$ , such artifacts arise from noise-induced amplification associated with the inversion of “small” singular values of  $\mathbf{H}$ . The corresponding singular vectors typically possess an oscillatory structure. Such difficulties also arise in the non-linear case such as the TWST problem considered here.

The second problem is computational. The nonlinearity of  $\mathbf{h}_i$  implies that an iterative, “hill-climbing” approach must be used to generate the reconstruction. As described in Section 4, such an approach requires the explicit inversion of  $\mathbf{I} - \mathbf{G}\mathcal{D}(\mathbf{g})$  at each iteration with  $\mathbf{g}$  equal to the current estimate of the object function. Because this matrix is both large and dense, this operation represents a substantial computational burden.

### 3. Wavelet Domain Model

We pursue a wavelet-based solution to the TWST problem to address both the computational and stability problems. The expansion of  $\mathbf{g}$  in a wavelet basis provides a natural mechanism for adapting the level of detail in the reconstruction to the information content in the data thereby stabilizing the solution procedure<sup>11,14</sup>. For example, near the center of  $A$ , one may only desire a coarse scale estimate of  $\mathbf{g}$  with added detail near the edges where the sharply peaked nature of the Green’s functions near the source and receiver locations provides the additional information. Also, the wavelet domain representations of  $\mathbf{L}_i$  and  $\mathbf{G}$  are sparse thereby lowering the computational costs associated with their manipulation. In the remainder of this section, we provide an overview of the wavelet transform and describe



the scale-space representation of the TWST problem. For simplicity, we limit most of the discussion to the one dimensional case. Extensions to multiple dimensions are obtained through the use of separable transforms<sup>18</sup>.

Like the Fourier series, a wavelet series represents a (square integrable) function as the superposition of a set of orthonormal functions. Whereas the Fourier basis employs complex exponentials, the wavelet basis is comprised of all dyadic dilations and shifts of a single wavelet function,  $\psi(x)$ , generally designed to be well localized in space. Thus, the wavelet expansion for a 1D function  $a(x)$  is:

$$a(x) = \sum_{j=-\infty}^{\infty} \sum_{k=-\infty}^{\infty} \alpha_{j,k} \psi_{j,k}(x) \quad (7)$$

where  $\psi_{j,k}(x) = 2^{-j/2} \psi(2^{-j}x - k)$  is the wavelet function at scale  $j$  and shift  $k$  and the wavelet coefficient  $\alpha_{j,k}$  is the inner product of  $a$  with  $\psi_{j,k}$ . Similarly to the complex exponentials, the wavelet functions form an orthonormal basis of the space of square integrable functions. In Fig. 2 we plot a number of the Daubechies 4-tap wavelet basis functions at different scales and positions. This picture illustrates that as  $j$  increases, the wavelet coefficients represent the inner product of  $a(x)$  with increasingly compressed basis functions and therefore convey localized, fine scale/high frequency information about  $a$  near the point  $2^{-j}k$ .

For most problems, we deal with truncated versions of the infinite sums. To truncate the scale index we introduce the *scaling function*,  $\phi(x)$ , which represents the coarse scale information from  $j = -\infty$  to some arbitrary, finite, coarse scale which we label  $j = 0$ . Because the  $\phi_{0,k}$  are orthonormal to one another, as well as the wavelets,  $\psi_{j,k}(x)$ , (7) becomes

$$a(x) = \sum_{k=-\infty}^{\infty} a_{0,k} \phi_{0,k}(x) + \sum_{j=0}^{F_a} \sum_{k=-\infty}^{\infty} \alpha_{j,n} \psi_{j,n}(x) \quad (8)$$

where the scaling coefficients  $a_{0,k}$  are the inner products of  $\phi_{0,k}(x)$  with  $a(x)$  and we have assumed that  $a(x)$  is “scale-limited” to  $j = F_a$ . Essentially, in this finite scale case, the scaling functions capture the low frequency behavior (including DC) of  $a(x)$ . The truncation of  $k$  required for considering functions defined on a bounded subset of the real line is achieved either through a process of periodization<sup>19</sup> or by using special “edge” wavelets built for

multiscale expansion on an interval<sup>20</sup>. Following our previous work<sup>11,14</sup>, here we use the edge wavelets approach as such an approach avoids any “wrapping” effects caused by linking one end of the interval to the other.

Like the Fourier case, there is an orthonormal discrete wavelet transform (DWT) which takes a vector of coefficients representing a function at some fine scale  $F_a$  into the wavelet coefficients at all scales  $0 \leq j \leq F_a - 1$  along with the coarse scale scaling coefficients,  $a_{0,k}$ . The initial, fine scale functions could be samples of the function, expansion coefficients,  $a_{F_a,k}$ , in a fine scale, scaling function expansion of  $a(x)$  etc. While we will be concerned both with one- and two-dimensional signals, we describe first the mechanics of the 1D DWT. We define  $\mathbf{a}$ , of dimension  $2^{F_a}$ , to be the vector of fine scale coefficient and will denote this vector by  $\mathbf{a}(M_a)$ , indicating that this is a representation of  $\mathbf{a}$  at the finest scale,  $M_a$ .

Beginning with  $\mathbf{a}(M_a)$ , a coarser approximation,  $\mathbf{a}(M_a - 1)$ , is obtained by passing  $\mathbf{a}(M_a)$  through a low-pass, finite impulse response filter and decimating the filtered output by a factor of 2. Thus  $\mathbf{a}(M_a - 1)$  is coarser than  $\mathbf{a}(M_a)$  in that the filtering and downsampling procedure has removed the high-frequency structure from the original signal, and  $\mathbf{a}(M_a - 1)$  is half as long as  $\mathbf{a}(M_a)$ . The detail lost in moving from  $\mathbf{a}(M_a)$  to  $\mathbf{a}(M_a - 1)$  (denoted  $\boldsymbol{\alpha}(M_a - 1)$ ) is extracted by a high-pass filter and decimation procedure. The filtering and decimation process is applied successively to the coarsened versions of  $\mathbf{a}$ , resulting in a sequence of scaling coefficient and detail vectors,  $\mathbf{a}(m)$  and  $\boldsymbol{\alpha}(m)$ , respectively, each of dimension  $2^m$ , for  $m = M_a - 1, \dots, 0$ .

Low and high pass filters, which are closely related to the functions  $\phi(x)$  and  $\psi(x)$ , can be constructed so that we may build an unitary matrix,  $\mathbf{W}_a$  relating the finest scale scaling coefficients to the coarsest scaling coefficients and all detail coefficients<sup>21</sup>. We note that not all wavelet transforms result in unitary DWT matrices. In particular, so-called bi-orthogonal DWTs possess a variety of advantages over their orthonormal counterparts<sup>22</sup>; however, in this paper, we consider only the orthonormal DWT. We subscript the wavelet transform operator as  $\mathbf{W}_a$  to make explicit that this is the transform for  $\mathbf{a}$ . We will use different wavelet transforms for the different variables.

The DWT of a two-dimensional function is obtained by considering the image,  $a(m, n)$ , as a matrix and applying one orthonormal wavelet transform,  $\mathbf{W}_{a,x}$ , to the columns and another,  $\mathbf{W}_{a,y}$ , to the rows. If we define  $\check{\mathbf{a}}$  as the physical-space image (that is,  $[\check{\mathbf{a}}]_{m,n} = a(m, n)$ ) and  $\check{\boldsymbol{\alpha}}$  as the 2D DWT of  $\check{\mathbf{a}}$  then the two are related according to

$$\check{\boldsymbol{\alpha}} = \mathbf{W}_{a,z} \check{\mathbf{a}} \mathbf{W}_{a,x}^T. \quad (9)$$

Note that  $\check{\boldsymbol{\alpha}}$  in (9) may be regarded as a multiscale “image” of  $\check{\mathbf{a}}$ . That is, the columns and rows of  $\check{\boldsymbol{\alpha}}$  are independently indexed by scale/shift indices for the  $x$  and  $y$  variables respectively. That is, the elements of  $\check{\boldsymbol{\alpha}}$  represent wavelet coefficients for discrete, separable, 2D basis functions comprised of wavelets at scale/shift  $(j_x, k_x)$  in the horizontal direction and  $(j_y, k_y)$  in the vertical for all allowable combinations of these four indices. Additionally, there are components of  $\check{\boldsymbol{\alpha}}$  corresponding to coarse scale,  $x$ -oriented scaling functions with vertical wavelets and vice versa. Finally, we note that (9) is a linear transformation of  $\check{\mathbf{a}}$ . Thus, we define vectors  $\mathbf{a}$  and  $\boldsymbol{\alpha}$  obtained by stacking one column on top of another from  $\check{\mathbf{a}}$  and  $\check{\boldsymbol{\alpha}}$  respectively and it is easily shown that

$$\boldsymbol{\alpha} = \mathbf{W}_a \mathbf{a}.$$

The matrix  $\mathbf{W}_a$  is the linear operator mapping elements of  $\mathbf{a}$  into elements of  $\boldsymbol{\alpha}$  and represents the composition of  $\mathbf{W}_{a,x}$  and  $\mathbf{W}_{a,y}$ . As in the 1D case,  $\mathbf{W}_a$  as defined above is unitary so that  $\mathbf{a}$  may be obtained from  $\boldsymbol{\alpha}$  via multiplication by the transpose of  $\mathbf{W}_a$ :  $\mathbf{a} = \mathbf{W}_a^{-1} \boldsymbol{\alpha} = \mathbf{W}_a^T \boldsymbol{\alpha}$ . Thus, by following this column-stacking approach, the mechanics and symbolic manipulation of multidimensional wavelet transforms is identical to the 1D case.

We use the DWT to transform (3) and (4) from physical space to scale space. Defining  $\mathbf{W}_g$  as the 2D transform for  $\mathbf{g}$  and  $\mathbf{W}_i$  for  $i = 1, 2, \dots, K$  as the 1D transforms for  $\mathbf{y}_i$  yields:

$$\begin{aligned} \mathbf{W}_i \mathbf{y}_i &= [\mathbf{W}_i \mathbf{L}_i \mathbf{W}_g^T] [\mathbf{W}_g \mathcal{D}(\mathbf{T}_i) \mathbf{W}_g^T] (\mathbf{W}_g \mathbf{g}) + \mathbf{W}_i \mathbf{n}_i \\ \mathbf{W}_i \mathbf{T}_i &= \mathbf{W}_i \bar{\mathbf{T}}_i + [\mathbf{W}_i \mathbf{G} \mathbf{W}_g^T] [\mathbf{W}_g \mathcal{D}(\mathbf{g}) \mathbf{W}_i^T] (\mathbf{W}_i \mathbf{T}_i) \end{aligned}$$

which, upon making the obvious definitions become

$$\boldsymbol{\eta}_i = \boldsymbol{\Lambda}_i \boldsymbol{\Delta}(\boldsymbol{\theta}_i) \boldsymbol{\gamma} + \boldsymbol{\nu}_i \quad (10)$$

$$\boldsymbol{\theta}_i = \bar{\boldsymbol{\theta}}_i + \boldsymbol{\Gamma} \boldsymbol{\Delta}(\boldsymbol{\gamma}) \boldsymbol{\theta}_i. \quad (11)$$

where, for example,  $\boldsymbol{\Delta}(\boldsymbol{\gamma})$  is the standard form<sup>12</sup> wavelet transform of  $\mathcal{D}(\mathbf{g})$  and is a function of  $\boldsymbol{\gamma}$  since  $\boldsymbol{\Delta}(\boldsymbol{\gamma}) = \mathbf{W}_g \mathcal{D}(\mathbf{W}_g^T \boldsymbol{\gamma}) \mathbf{W}_g^T$ . From (10) and (11), the complete model relating the transform of the object to those of the data is

$$\boldsymbol{\eta}_i = \underbrace{\boldsymbol{\Lambda}_i \boldsymbol{\Delta} [(\mathbf{I} - \boldsymbol{\Gamma} \boldsymbol{\Delta}(\boldsymbol{\gamma}))^{-1} \bar{\boldsymbol{\theta}}_i]}_{\boldsymbol{\Upsilon}_i(\boldsymbol{\gamma})} \boldsymbol{\gamma} + \boldsymbol{\nu}_i. \quad (12)$$

Finally, we aggregate the  $\boldsymbol{\eta}_i$  into a single data vector and define the stacked system

$$\boldsymbol{\eta} = \boldsymbol{\Upsilon}(\boldsymbol{\gamma}) + \boldsymbol{\nu} \quad (13)$$

with  $\boldsymbol{\eta} = [\boldsymbol{\eta}_1^T \dots \boldsymbol{\eta}_K^T]$  and  $\boldsymbol{\Upsilon}(\boldsymbol{\gamma})$  and  $\boldsymbol{\nu}$  defined accordingly. With (13), the TWST inverse problem to be solved here is the recovery of  $\boldsymbol{\gamma}$ , the DWT of  $\mathbf{g}$ , from measurements  $\boldsymbol{\eta}$ , knowledge of  $\boldsymbol{\Upsilon}$ , and the statistics of  $\boldsymbol{\nu}$ .

#### 4. Inversion Algorithm

In this paper, the reconstruction of  $\boldsymbol{\gamma}$ , denoted by  $\hat{\boldsymbol{\gamma}}$ , given the data,  $\boldsymbol{\eta}$ , is defined to be the solution to the following non-linear least squares type of optimization problem

$$\hat{\boldsymbol{\gamma}} = \arg \min_{\boldsymbol{\gamma}} \mathcal{C}(\boldsymbol{\gamma}) \quad (14)$$

$$\mathcal{C}(\boldsymbol{\gamma}) = \frac{1}{2} \|\boldsymbol{\eta} - \boldsymbol{\Upsilon}(\boldsymbol{\gamma})\|_{\mathcal{R}^{-1}}^2 + \lambda^2 \rho^T(\boldsymbol{\gamma}) \rho(\boldsymbol{\gamma}) \quad (15)$$

where  $\|\mathbf{x}\|_{\mathbf{A}} \equiv \mathbf{x}^T \mathbf{A} \mathbf{x}$ ,  $\mathcal{R}$  is a diagonal weighting matrix whose entries reflect the noise levels in the data and  $\rho^T(\boldsymbol{\gamma}) \rho(\boldsymbol{\gamma})$  is used to regularize the problem. The process of minimizing the computational cost function,  $\mathcal{C}(\boldsymbol{\gamma})$ , forces  $\hat{\boldsymbol{\gamma}}$  to balance the effects of the two terms comprising  $\mathcal{C}$ . The first term enforces fidelity to the data. That is, our choice of  $\hat{\boldsymbol{\gamma}}$  should be such that when put through the forward model,  $\boldsymbol{\Upsilon}$ , it comes “close” to reproducing the data,  $\boldsymbol{\eta}$ , where closeness is measured in the appropriate norm. Thus, smaller cost is associated with reconstructions which better explain the data that we have collected.

Were the first term in (15) the only portion of the cost, the ill-posed nature of the TWST problem would result in a reconstruction with large amplitude, high frequency components. To counter this effect, the regularization term,  $\rho^T \rho$ , is included. Generally  $\rho^T \rho$  is used to constrain the reconstruction to have properties such as small energy (i.e. small  $L_2$  norm), minimal gradient norm, or other smoothness-type of characteristics<sup>23</sup>. Hence, vectors corresponding to such oscillatory reconstructions are less desirable and therefore incur a higher cost. Finally,  $\lambda^2$ , the regularization parameter, is specified to balance the relative impact of the two terms on the reconstruction procedure. To summarize, the overall problem is to find a vector  $\hat{\gamma}$  which minimizes a cost function. This function imposed higher cost (i.e. higher computational penalty) for  $\gamma$  which fails to replicate the measured data and which possesses unfavorable structure, such as oscillatory behavior.

We employ a form of the Levenberg-Marquardt algorithm (LMA)<sup>24</sup> for finding  $\hat{\gamma}$ . This iterative technique defines a sequence of reconstructions,  $\hat{\gamma}_n$ , whose costs as measured by (15) are steadily decreasing. Starting from an initial guess,  $\hat{\gamma}_0$ , the form of the LMA used here is

$$\hat{\gamma}_{n+1} = \hat{\gamma}_n + \mathbf{s}_n \quad (16)$$

$$\mathbf{s}_n = \arg \min_{\sigma^2} \mathcal{C}(\hat{\gamma}_n + \mathbf{s})$$

$$\mathbf{s} = [\mathcal{J}^T(\hat{\gamma}_n) \mathcal{R}^{-1} \mathcal{J}^T(\hat{\gamma}_n) + \sigma^2 \mathcal{L}^T(\hat{\gamma}_n) \mathcal{L}(\hat{\gamma}_n)]^{-1} \times \\ \mathcal{J}^T(\hat{\gamma}_n) \mathcal{R}^{-1} [\boldsymbol{\eta} - \mathbf{Y}(\hat{\gamma}_n)] - \mathcal{L}^T(\hat{\gamma}_n) \mathcal{L}(\hat{\gamma}_n). \quad (17)$$

In (17),  $\mathcal{J}(\hat{\gamma}_n)$  is the Jacobian matrix of  $\mathbf{Y}$  evaluated at the vector  $\hat{\gamma}_n$ . To build the  $(j, k)$ th element of  $\mathcal{J}$ , the  $j$ th component of  $\mathbf{Y}$  is differentiated with respect to the  $k$ th element of  $\gamma$ . This scalar function will, in general, depend on all components of  $\gamma$ . The Jacobian is obtained by evaluating each such derivative at the point  $\gamma = \hat{\gamma}$ . Similarly  $\mathcal{L}(\hat{\gamma}_n)$  is the Jacobian of  $\rho$  evaluated at  $\hat{\gamma}_n$ . Finally,  $\sigma$  is a regularization parameter whose value is determined adaptively at each iteration of the algorithm.

In the remainder of this section, we discuss the choice of  $\rho$ , an approximation to the forward model designed to reduce the complexity of the LMA including the construction of  $\mathcal{J}$ , and overview the computational burden of this inversion approach.

## A. Edge Preserving Wavelet Regularization

In our previous work<sup>11,14</sup>, we have concentrated on the use of wavelet domain regularizers with  $\rho(\gamma) = \mathbf{D}\gamma$  where the matrix  $\mathbf{D}$  was diagonal with

$$[\mathbf{D}]_{ii} \equiv d_i = 2^{-(\alpha_x j_{x,i} + \alpha_y j_{y,i})}. \quad (18)$$

In (18)  $j_{x,i}$  and  $j_{y,i}$  are the horizontal and vertical scale indices for the  $i$ th wavelet coefficient and  $\alpha_x$  and  $\alpha_y$  are constants. For this regularization approach,  $\rho^T(\hat{\gamma}_n)\rho(\hat{\gamma}_n)$  is a weighted two-norm of  $\hat{\gamma}_n$ . This choice of  $\rho$  enforces smoothness in the reconstruction and functions in much the same way as traditional Tikhonov type regularizers<sup>11,14</sup>. One consequence of this choice is that edges and other sharp discontinuities which may be of interest in localizing defects or quantitatively characterizing their structure tend to be blurred in the final reconstruction.

Recently, there has been considerable work performed in the area of “edge-preserving” regularizers<sup>25,26</sup>. The idea is to construct a physical-space regularization scheme which results in reconstructions whose discontinuities are better preserved as compared to a Tikhonov approach. One way of implementing this regularization technique is to choose an expression for  $\rho^T\rho$  which, instead of being a weighted two-norm of the object, is a norm in a function space containing “edgy” objects. Adding this as the second term in (15) produces an object which lies in such a space and therefore retains the desired edge-like structure.

It is the case that, in addition to spanning the space of square integrable functions, orthonormal wavelets are also bases for these more exotic function spaces<sup>16</sup>. Here we make use of the fact that the norm in such a space may be computed in terms of the wavelet coefficients via  $\sum_i d_i |\gamma_i|^p$  with  $1 \leq p \leq 2$  and  $d_i$  exactly the same as in (18).

The use of  $p$  in this range to describe edge characteristics is best described using a one dimensional example. In Fig. 3, we plot a 1D signal with two edges along with the wavelet coefficients of this signal over a collection of scales. The original function is the topmost trace and each box on the subsequent traces represents a single wavelet coefficient at a given scale.

Finest scale coefficients are closest to the top of the picture. These sequences are basically zero except for coefficients describing the behavior of the function near the edges of the step where there are “spikes.” Thus, the wavelet sequences provide localized information about the discontinuity structure (i.e. local smoothness) of the underlying function. If we were attempting to reconstruct such a signal, the cost of the spikes as measured by the regularization term,  $\sum_i d_i |\gamma_i|^p$ , decreases as  $p$  drops from 2 to 1. In other word, a  $p = 2$  regularization scheme seeks smooth reconstructions and thus penalizes the presence of such spikes thereby resulting in blurry reconstruction. By taking  $p < 2$ , the cost of the spikes is smaller and the reconstruction should more faithfully reproduce the underlying edges.

With this motivation, we make the following choice for  $\rho(\gamma)$

$$\rho^T(\gamma) = \begin{bmatrix} d_1^{1/2} |\gamma_1|^{p/2} & d_2^{1/2} |\gamma_2|^{p/2} & \dots & d_N^{1/2} |\gamma_N|^{p/2} \end{bmatrix} \quad (19)$$

which results in a diagonal  $\mathcal{L}$  with

$$[\mathcal{L}(\hat{\gamma}_n)]_{i,i} = d_i^{1/2} \frac{p}{2} l([\hat{\gamma}_n]_i) \quad (20)$$

$$l(x) = \text{sign}(x) |x|^{p/2-1} \quad (21)$$

where  $[\hat{\gamma}_n]_i$  is the  $i$ th element of the vector  $\hat{\gamma}_n$ .

As seen from the plot of  $l(x)$  in Fig. 4, the presence of a singularity at  $x = 0$  will lead to numerical difficulties when implementing this regularization scheme. For the examples in Section 5, we replace  $l(x)$  with the function  $\bar{l}(x)$  defined as

$$\bar{l}(x) = \frac{x}{\epsilon + |x|^{2-p/2}}. \quad (22)$$

where  $\epsilon$  is a small positive number governing the structure of  $\bar{l}(x)$  for  $x \approx 0$ . For example Fig. 4 shows that for  $p = 1.2$  and  $\epsilon = 10^{-3}$ ,  $\bar{l}(x)$  is better behaved around the origin while still retaining the essential shape of  $l(x)$ . Also,  $\bar{l}(x)$  possesses the same asymptotic structure as  $l(x)$  for  $|x| \gg 0$ . Taken together, these facts indicate that  $\bar{l}(x)$  should perform comparably to  $l(x)$  in the LMA.

## B. Approximate Physical Model

Two factors related to the forward scattering model dominate the computational complexity of the LMA. The first component is the evaluation of  $\Upsilon(\hat{\gamma}_n)$  as required by (17). According to (12), this problem requires the inversion of  $[\mathbf{I} - \Gamma\Delta(\hat{\gamma}_n)]$ . The quantity  $\Xi_n \equiv [\mathbf{I} - \Gamma\Delta(\hat{\gamma}_n)]^{-1}$  has the interpretation as the wavelet transform of the discretized resolvent associated with the second kind integral equation (2) with  $g(\mathbf{r})$  equal to the estimate of the object function at the  $n$ th iteration of the LMA.

The second computationally intensive task is the construction of  $\mathcal{J}(\hat{\gamma}_n)$ . To obtain an expression for  $\mathcal{J}(\hat{\gamma}_n)$  we note first that this matrix is built by “stacking”  $\mathcal{J}_i(\hat{\gamma}_n)$ , the Jacobian matrices for the  $K$  scattering experiments. For an arbitrary  $\gamma$ ,  $\mathcal{J}_i(\gamma)$  is<sup>27</sup>

$$\mathcal{J}_i(\gamma) = \Lambda_i \Delta(\theta_i) + \Lambda_i [\mathbf{I} - \Gamma\Delta(\gamma)]^{-1} \Gamma\Delta(\theta_i) \quad (23)$$

with  $\theta_i = [\mathbf{I} - \Gamma\Delta(\gamma)]^{-1} \bar{\theta}_i$ . The construction of  $\mathcal{J}_i$  clearly requires a number of matrix multiplications and, like the evaluation of  $\Upsilon_i$ , the inversion of  $\mathbf{I} - \Gamma\Delta(\gamma)$ . While the matrix-matrix multiplications can be computationally intensive the relevant matrices are sparse thereby reducing the time overhead of this task (see Section 4 C). Thus, our primary concern here is to develop a method which avoids the need to explicitly invert  $\mathbf{I} - \Gamma\Delta(\gamma)$  as such an approach aids both in evaluating  $\Upsilon$  and in building the Jacobian.

The method we propose is based on the observation that at the beginning of stage  $n + 1$  of the LMA, we require

$$\Xi_{n+1} \equiv [\mathbf{I} - \Gamma\Delta(\hat{\gamma}_{n+1})]^{-1} = [\mathbf{I} - \Gamma\Delta(\hat{\gamma}_n + \mathbf{s}_n)]^{-1}$$

where the second equality follows from (16) and where  $\mathbf{s}_n$  is typically a small correction to  $\hat{\gamma}_n$ . Making use of the fact that  $\Delta$  is a linear operator

$$\Xi_{n+1} = [\mathbf{I} - \Gamma\Delta(\hat{\gamma}_n + \mathbf{s}_n)]^{-1} = [\mathbf{I} - \Gamma\Delta(\hat{\gamma}_n) - \Gamma\Delta(\mathbf{s}_n)]^{-1} \quad (24)$$

$$= \Xi_n [\mathbf{I} - \Gamma\Delta(\mathbf{s}_n)\Xi_n]^{-1} \quad (25)$$

$$\approx \Xi_n + \Xi_n \Gamma\Delta(\mathbf{s}_n)\Xi_n \quad (26)$$



where (26) follows from (24) under the assumption that  $\mathbf{\Gamma}\mathbf{\Delta}(\mathbf{s}_n)\mathbf{\Xi}_n$  is “small” relative to  $\mathbf{I}$  and  $\mathbf{\Xi}_n$  is given by  $[\mathbf{I} - \mathbf{\Gamma}\mathbf{\Delta}(\hat{\gamma}_n)]^{-1}$

As an approximation to  $\mathbf{\Xi}_{n+1}$ , (26) possesses some interesting and useful properties. First, we note that, unlike the Born approximation, this is not a linearization of the physics about the current estimate of the object function. Indeed, while (26) *is* linear in the increment,  $\mathbf{s}_n$ , the presence of the two  $\mathbf{\Xi}_n$  in the second terms make it quadratic in  $\hat{\gamma}_n$ . Second, because the left hand side of (24) is, by definition,  $\mathbf{\Xi}_{n+1}$  our approximation provides a recursive method for updating the resolvent from one iteration of the LMA to the next. Specifically, we have

$$\mathbf{\Xi}_{n+1} = \mathbf{\Xi}_n + \mathbf{\Xi}_n \mathbf{\Gamma} \mathbf{\Delta}(\mathbf{s}_n) \mathbf{\Xi}_n \quad (27)$$

which states that the new resolvent is equal to the old resolvent plus an increment which is a function both of  $\mathbf{\Xi}_n$  as well as  $\mathbf{s}_n$ , the update to the reconstruction at iteration  $n$ .

### C. Computational Considerations

Each iteration of the LMA defined by (16)-(17) requires first the construction of  $\mathbf{\Upsilon}(\hat{\gamma}_n)$ ,  $\mathcal{J}(\hat{\gamma}_n)$ , and  $\mathcal{L}(\hat{\gamma}_n)$  and then the solution of a sequence of least-squares type problems to determine  $\mathbf{s}_n$ . According to (20), determining  $\mathcal{L}(\hat{\gamma})$  requires roughly  $2N$  floating point operations. While the need to solve the least squares problems can be intensive, we have previously developed techniques based on our wavelet representation for  $\mathbf{g}$  for reducing the computational overhead of this task<sup>11</sup>. As discussed in the previous section the computational costs of the remaining tasks, evaluating  $\mathbf{\Upsilon}$  and building  $\mathcal{J}$ , are dominated by the need to compute  $\mathbf{\Xi}_n$ .

By using (27), we replace the matrix inversion by three matrix-matrix products. The primary reduction in computational complexity comes from the fact that these matrices are sparse by construction (e.g.  $\mathbf{\Delta}(\hat{\gamma}_n)$ )<sup>11</sup> or can be made so with little loss (eg.  $\mathbf{\Gamma}$  and  $\mathbf{\Xi}_n$ ) by truncating small elements. While it is not necessarily the case that products of

sparse matrices are themselves sparse, we ensure sparsity and therefore low complexity by implementing (27) as

$$\Xi_{n+1} = \text{trunc}_\delta [\Xi_n + \text{trunc}_\delta [\Xi_n \Gamma] \text{trunc}_\delta [\Delta(\hat{\gamma}_n) \Xi_n]]$$

where, for a matrix  $\mathbf{M}$ ,  $\text{trunc}_\delta(\mathbf{M})$  is the sparse approximation to  $\mathbf{M}$  via the method in Ref. [28] with a threshold  $\delta$ . Under this truncation scheme we set to zero all elements of the  $m \times n$  matrix  $\mathbf{M}$  whose absolute values are less than  $\frac{\delta}{n} \|\mathbf{M}\|_\infty$ .

## 5. Examples of Thermal-Wave Tomographic Imaging

To illustrate the inversion algorithm developed in the previous sections, we consider the imaging of single and multiple defects in a 3 mm by 3 mm block of aluminum (thermal diffusivity of  $0.82 \text{ cm}^2\text{s}^{-1}$ ). Depending on the example, the reconstructions are based on the individual or joint processing of backpropagation and transmission data collected for one or more locations of the modulated heating laser equally spaced across the top of the material sample. A given transmission or backpropagation data set consists of measurements of noisy scattered fields obtained at 32 equally spaced points along either the top or the bottom of the material. For all cases, the top of the sample is taken to be the line  $x = 0$  while the bottom is at  $x = 3\text{mm}$ . The angular modulation frequency of the laser for all experiments is taken to be 8 Hz. Finally, the signal to noise ratio in decibels (dB) for the  $i$ th experiment is defined as

$$SNR_i = 10 \log_{10} \frac{\|\mathbf{h}(\mathbf{g})\|_2^2}{N_i q_i^2}$$

where  $q_i^2$  is the variance of the  $i$ th noise process,  $N_i$  is the number of data points in the  $i$ th data vector and  $\mathbf{h}(\mathbf{g}) = [\mathbf{h}_1^T(\mathbf{g}) \ \mathbf{h}_2^T(\mathbf{g}) \ \dots \ \mathbf{h}_K^T(\mathbf{g})]$  with  $\mathbf{h}_i(\mathbf{g})$  given by (6).

For purposes of inversion, we seek a reconstruction of  $g$  on a  $16 \times 16$  grid. A Haar wavelet<sup>22</sup> is used to transform both the data vectors as well as  $\mathbf{g}$ . The parameter  $\lambda^2$  in (15) is 10 and  $\alpha_x = \alpha_y = 1$  in the regularization method. The value of  $\delta$  used to truncate the operators is 0.01. These quantities were chosen by trial and error. The quality of the reconstructions

was relatively insensitive to the choices for  $\alpha_x$ ,  $\alpha_y$ , and  $\delta$ . Choosing the correct value for the regularization parameter  $\lambda^2$  can be a delicate procedure. For the TWST examples presented here, values between 1 and 100 tended to produce similar results. We leave for future efforts the development of a more automated procedure for selecting this parameter.

To verify the utility of the edge-preserving regularization method, we examine reconstructions obtained with both  $p = 2$  and  $p = 1.2$  in (22). The  $p = 2$  case corresponds to the wavelet-domain smoothness regularization previously employed<sup>11,14</sup>, while the  $p = 1.2$  selection will be shown to result in more accurately recovered edges. For the  $p = 2$  reconstructions, the LMA is initialized with  $\hat{\gamma}_0 = 0$ . For the  $p = 1.2$  case, we first run the LMA with  $p = 2$  for 3 iterations and then switch to  $p = 1.2$  for the remainder of the reconstruction process. This strategy avoids instabilities associated with the sharp transition of the  $p = 1.2$  regularization function which can arise when the LMA is seeded with the zero vector. Finally, by starting the LMA with zero, the first iteration of the algorithm is mathematically equivalent to reconstruction under the Born approximation using the  $p = 2$  wavelet domain regularizer. Thus, we can compare the reconstructions for the non-linear algorithm to those obtained when a Born model with wavelet regularization is used to process the data.

The first example we consider is the reconstruction of a square air hole centered near the top of the sample. The object function for this case is shown in Fig. 5(a) and consists of a square hole of amplitude<sup>4,5</sup>  $(\alpha_{\text{AI}}/\alpha_{\text{air}}) - 1 \approx 3$ . The SNR for all experiments is 50dB. The reconstruction obtained under the Born approximation is displayed in Fig. 5(b). For this case, the Born approximation yields coarse-scale localization of the defect. That is, the reconstruction is non-zero over a region of space which includes the area of the true defect. However, the amplitude of the reconstruction is at best a third of the true amplitude and the shape of the reconstructed defect is in fact larger than that of the true structure. The execution time for the Born algorithm on a Sparc 20 was about 11 minutes with much of this time devoted to the search for the optimal regularization parameter  $\sigma$  in (17). To summarize, the Born reconstruction provides relatively fast access to an image which provides a rough idea as to the location of the defect with little information regarding the amplitude.

The final results of the of the  $p = 2$  and  $p = 1.2$  LMA are shown in Figs. 5(b), (c), and (d) respectively. In Fig. 5(e), the value of  $\|\hat{\gamma}_n - \gamma\|_2$  is plotted for both regularization schemes as a function of iteration. It is evident that both regularization schemes produce reconstructions which are better localized with more accurate amplitude information than the Born inversion. The  $p = 1.2$  case is slightly better than the  $p = 2$  reconstruction both from a quantitative and qualitative perspective. Quantitatively, the error in the  $p = 1.2$  estimate is somewhat lower than that of the  $p = 2$  case after 10 iterations. This improvement is due to the fact that the  $p = 2$  case overestimates the amplitudes in a couple of pixels, while the amplitude of the  $p = 1.2$  version is quite accurate. Visually, as we expect, the edges on the  $p = 1.2$  reconstruction are sharper and the overall reconstruction looks much more like a box than a smoothed blob as is the case in Fig. 5(c). The price paid for the increase in the accuracy of both reconstructions relative to the Born case is primarily computational. The processing time for both LMA reconstruction of this  $16 \times 16$  grid of pixels is on the order of 2 hours again using a Sparc 20.

In Fig. 6, the utility of jointly processing both transmission and backpropagation data is illustrated. In all cases, we use the same object as before and  $p = 1.2$  regularization. The final reconstructions obtained using only backpropagation data is displayed in Figs. 6(b). Here we see that the object is relatively well localized and the edges are nicely captured; however the reconstruction of the rear portion of the defect is clearly inferior to that obtained when both transmission and backpropagation data are employed (Fig. 6(d)). Indeed, this result is not unexpected given that the rear of the defect is effectively shadowed for the backpropagation case.

The transmission only reconstruction is shown in Fig. 6(c). This image is significantly more blurred than the other two despite the use of edge-preserving regularization. The longer propagation distances from sources to receivers effectively remove from the data most all of the fine scale information about the object function resulting in a severely degraded reconstruction. The results of using both transmission and backpropagation data are seen in Fig. 6(d). This reconstruction combines the best features of the other two. The object

and its edges are well localized like the backpropagation reconstruction while the use of the transmission data aids in improving the resolution of the back side of the defect. These advantages are seen as well in the error curves of Fig. 6(e). The transmission only inversion is clearly inferior to both of the others. While the backpropagation produces lower error reconstructions in the opening iterations, the joint inversion is ultimately superior.

The second example we consider is the reconstruction of a square hole located near the bottom of the material sample at an SNR of 50dB. As seen in Fig. 7, the structure of this defect is identical to that of the previous example, except for the location. In Figs. 7(b)–(e) we again plot the Born reconstructions, the final estimates obtained using the  $p = 2$  and 1.2 regularizations and the error as a function of iteration. As in the previous case, the Born estimate provides rough localization of the underlying defect with limited quantitative accuracy. For both regularization schemes, the final reconstructions improve significantly on the Born inversion. The final results for the  $p = 1.2$  case are however better than the  $p = 2$  estimate in capturing the sharp edges in the defect and in providing a flat top to the estimated object function.

As a final test, we demonstrate the performance of our approach in resolving adjacent sub-surface defects on an example with two square defects located near the center of the material shown in Fig. 8(a). As seen in panel (b) of this figure, the Born inversion basically indicates that there is some gross disturbance located near the center of the region. While the top anomaly (i.e. the structure nearer to the line  $x = 0$ ) is slightly better captured than the bottom, in neither case is the amplitude well represented.

Fig. 8(c)–(d) shows that the non-linear inversion routine is quite capable of resolving both structures and in providing quantitatively accurate contrast information. As was seen in the previous two examples, the  $p = 2$  reconstruction is smoother than the  $p = 1.2$  case and is slightly less accurate in terms of the amplitudes of the defects. For the  $p = 1.2$  reconstruction, the back defect is quite well localized in space and has a close to flat contrast. The front structure is well defined in its  $y$  variation with less accuracy in  $x$ . The amplitude of this reconstruction is again quite flat with sharp, well defined edges. The defects are well

resolved in both the  $p = 2$  and  $p = 1.2$  reconstructions. Quantitatively, the error in the  $p = 1.2$  estimate is lower than that of the  $p = 2$  case after 7 iterations.

## 6. Conclusions and Future Work

We have presented a new approach to image formation from scattered thermal waves based on the use of non-linear inverse scattering methods and wavelet-domain techniques. We build out inversion routine on the full wavefield physics developed by Mandelis in Ref. [ 4, 5] resulting in a highly non-linear relationship between the data on which a reconstruction is to be based and the desired image of the object function. The reconstruction problem was formulated as a solution to a non-linear least-squares type optimization problem in the wavelet transform domain. We chose to work in a multiscale setting for a number of reasons. First, the matrices comprising the physical model are sparse in this domain thereby lowering the computational cost of generating a reconstruction. Second, we were able to make use of a new class of edge-preserving regularization methods which are easily specified and implemented in the wavelet transform domain. Finally, the computational burden was further reduced by employing the methods of Ref. [ 11] for rapidly solving non-linear inverse scattering problems in a multiscale domain.

The Levenberg-Marquardt algorithm formed the basis for the inversion procedure. This approach provided a natural mechanism for the joint processing of data from an arbitrary number of scattering experiments. Thus, rather than forming separate images for each source-receiver array combination and then averaging the results, we were able to produce a single image which was optimal across all data sets.

A key component of this inversion technique was shown to be the explicit inversion of the resolvent for the forward scattering model at each iteration of the algorithm. This matrix was required for the calculation of the Jacobian and played a central role in evaluating the data-misfit at every stage of the reconstruction. We introduced a new approximation to this resolvent which replaced the need to explicitly invert a generally large matrix with only

the requirement of multiplying a sequence of three matrices. The complexity of even this operation was further reduced via our wavelet approach where the sparse matrix structure could be exploited.

The algorithm was demonstrated for imaging defects in the bulk structure of an aluminum sample using thermal wave slice tomography. Inversions were considered in which synthetic transmission and backpropagation scattering data were both input to the algorithm. Our results indicated that the use of the non-linear approach produces reconstructions which are significantly more accurate than a Born-based inversion both in terms of localization of the defects and obtaining quantitative contrast information. Additionally, relative to traditional Tikhonov-type regularizers, the edge-based regularization scheme produced reconstructions which better represented the block-like nature of the defects.

## **7. Acknowledgments**

The work of the first author was supported in part DOE contract DE-FC07-95ID13395, NSF Grant MIP-9623721, and by subcontract GC123920NDG from Boston University under the AFOSR MURI Program on Reduced Signature Target Recognition. The work of the other authors was supported by the Natural Sciences and Engineering Research Council of Canada, through a Research Grant.

## REFERENCES

1. L. Nicolaides and A. Mandelis, “Image-enhanced thermal-wave slice diffraction tomography with numerically simulated reconstructions: Theoretical and computational,” *Inverse Problems* (in press).
2. L. Nicolaides, M. Munidasa, and A. Mandelis, “Image-enhanced thermal-wave slice diffraction tomography with backpropagation and transmission reconstructions: Experimental,” *Inverse Problems* (in press).
3. O. Pade and A. Mandelis, “Computational thermal-wave slice tomography with backpropagation and transmission reconstructions,” *Rev. Sci. Instrum.* **64**, 3548–3562 (1993).
4. A. Mandelis, “Theory of photothermal-wave diffraction and interference in condensed media,” *J. Opt. Soc. Am.* A6 (1989).
5. A. Mandelis, “Green’s functions in thermal-wave physics: Cartesian coordinate representations,” *J. Appl. Phys.* **78**, 647–655 (1995).
6. C. Torres-Verdín and T. M. Habashy, “Rapid 2.5-D Forward Modeling and Inversion via a New Nonlinear Scattering Approximation,” *Radio Sci.* **29**, 1051–1079 (1994).
7. T. M. Habashy, W. C. Chew, and E. Y. Chow, “Simultaneous reconstruction of permittivity and conductivity profiles in a radially inhomogeneous slab,” *Radio Sci.* **21**, 635–645 (1986).
8. T. Wang, M. Oristaglio, A. Tripp, and G. Hohmann, “Inversion of diffusive transient electromagnetic data by a conjugate-gradient method,” *Radio Sci.* **29**, 1143–1156 (1994).
9. O. Pade and A. Mandelis, “Thermal-wave slice tomography using wave-field reconstruction,” *Inverse Problems* **10**, 185–197 (1994).



10. T. M. Habashy, R. W. Groom, and B. R. Spies, “Beyond the Born and Rytov Approximations: A Nonlinear Approach to Electromagnetic Scattering,” *J. Geophys. Res.* **98**, 1759–1775 (1993).
11. E. L. Miller and A. S. Willsky, “Wavelet-Based Methods for the Nonlinear Inverse Scattering Problem Using the Extended Born Approximation,” *Radio Sci.* **31**, 51–67 (1996).
12. G. Beylkin, R. Coifman, and V. Rokhlin, “Fast Wavelet Transforms and Numerical Algorithms, I,” *Commun. Pure Appl. Math.* **44**, 141–183 (1991).
13. M. Bertero, “Linear Inverse and Ill-Posed Problems,” in *Advances in Electronics and Electron Physics*, H. Peter W, ed., (Academic Press, Boston, 1989), Vol. 75, pp. 1–120.
14. E. L. Miller and A. S. Willsky, “Multiscale, Statistically-Based Inversion Scheme for the Linearized Inverse Scattering Problem,” *IEEE Trans. Geosc. Remote Sens.* **34**, 346–357 (1996).
15. M. Bertero, C. D. Mol, and E. R. Pike, “Linear inverse problems with discrete data, II, Stability and regularisation,” *Inverse Probl.* **4**, 573–594 (1988).
16. Y. Meyer, *Wavelets and Operators* (Cambridge, Cambridge, England, 1995).
17. R. F. Harrington, *Field Computations by Moment Methods* (Macmillan, New York, 1968).
18. B. Wang, J. C. Moulder, and J. P. Basart, “Wavelets in the solution of the volume integral equation: Application to eddy current modeling,” *J. Appl. Phys.* **81**, 6397–6406 (1997).
19. M. V. Wickerhauser, *Adapted wavelet analysis from theory to software* (A.K. Peters, Wellesley, MA, 1994).
20. A. Cohen, I. Daubechies, B. Jawerth, and P. Vial, “Multiresolution analysis, wavelets

- and fast algorithms on an interval,” *Appl. Comp. Harmonic Analysis* **1**, 54–81 (1993).
21. I. Daubechies, “Orthonormal Bases of Compactly Supported Wavelets,” *Commun. Pure Appl. Math.* **41**, 909–996 (1988).
  22. G. Strang and T. Nguyen, *Wavelets and Filter Banks* (Wellesley-Cambridge Press, Wellesley, MA, 1996).
  23. M. Bertero, C. D. Mol, and E. R. Pike, “Linear inverse problems with discrete data. I: General formulation and singular system analysis,” *Inverse Problems* **1**, 301–330 (1985).
  24. P. E. Gill, W. Murry, and M. H. Wright, *Practical Optimization* (Academic, San Diego, Calif., 1981).
  25. A. Gersztenkorn, J. B. Bednar, and L. R. Lines, “Robust Iterative inversion for the one-dimensional acoustic wave equation,” *Geophysics* **51**, 357–368 (1986).
  26. P. Charbonnier, L. Blanc-Feraud, G. Aubert, and M. Barlund, “Deterministic Edge-Preserving Regularization in Computed Imaging,” *IEEE Trans. Image Processing* **6**, 298–311 (1997).
  27. E. L. Miller, “The Application of Multiscale and Statistical Techniques to the Solution of Inverse Problems,” Technical Report No. LIDS-TH-2258, MIT Lab. for Information and Decision Syst., Cambridge, Mass. (1994) .
  28. B. Alpert, G. Beylkin, R. Coifman, and V. Rokhlin, “Wavelets for the Fast Solution of Second-Kind Integral Equations,” *SIAM J. Sci. Comput.* **14**, 159–184 (1993).

## 8. Figure Captions

- **Fig. 1:** Experimental setup for thermal wave slice tomography. Incident thermal waves originating from a point on the top of the material sample interact with defects giving rise to scattered fields whose effects are measured by arrays located at the top and bottom of the sample. The objective of the inverse problem is to image the internal structure of the material based on these measurements. The incident point is generally scanned across the top.
- **Fig. 2:** Plots of Daubechies 4-tap wavelet basis functions. Solid line =  $\psi_{4,1}(x)$ , dash line =  $\psi_{4,3}(x)$ , dot-dash line =  $\psi_{5,13}(x)$ , and dotted line =  $\psi_{5,17}(x)$ .
- **Fig. 3:** Wavelet transform of a pulse function. The original function is given by the top trace and the wavelet coefficients at a variety of scales are shown in the lower traces. Finer scale information is conveyed in traces closer to the top. The wavelet coefficients characterize the local discontinuity structure of the function.
- **Fig. 4:** Plot of  $l(x)$ (dashed) and  $\bar{l}(x)$  (solid) used to implement wavelet-domain edge preserving regularization. Both functions are identical for  $x \gg 0$ , but  $\bar{l}(x)$  is better behaved near the origin thereby aiding in numerical implementation.
- **Fig. 5:** True object function, inversion results and error vs. iteration for single defect located near the top of the material. The laser source position is along the line  $x = 0$ .
- **Fig. 6:** True object function, inversion results and error vs. iteration for single defect located near the top of the material. Here we compare reconstructions obtained using only backpropagation data (b), only transmission data (c) and a combination of both (d) in the non-linear inversion algorithm. The laser source position is along the line  $x = 0$ .
- **Fig. 7:** True object function, inversion results and error vs. iteration for single defect located near the bottom of the material. The laser source position is along the line

$x = 0$ .

- **Fig. 8:** True object function, inversion results and error vs. iteration for two-defect problem. The laser source position is along the line  $x = 0$ .

FIGURES

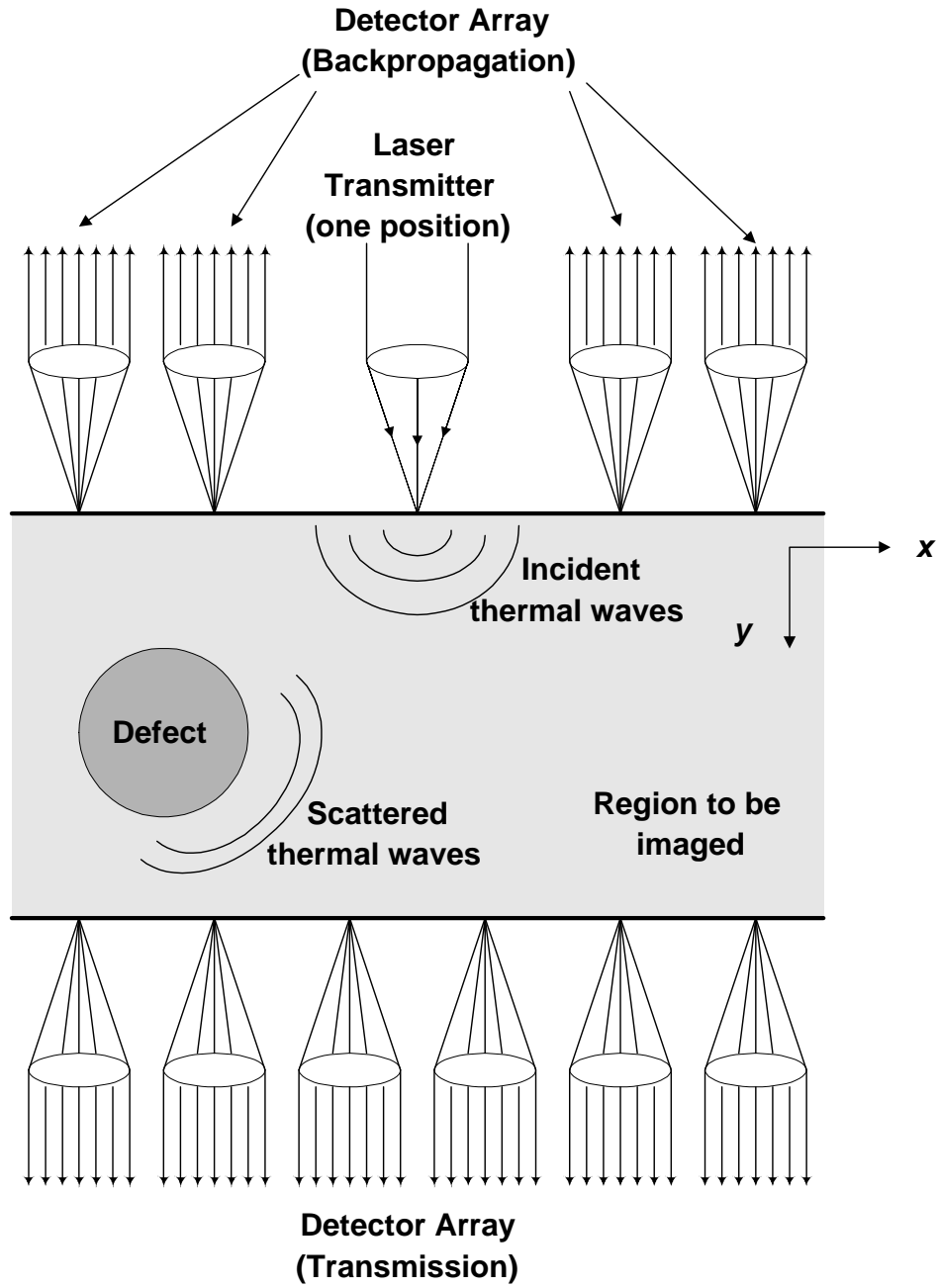


Fig. 1.

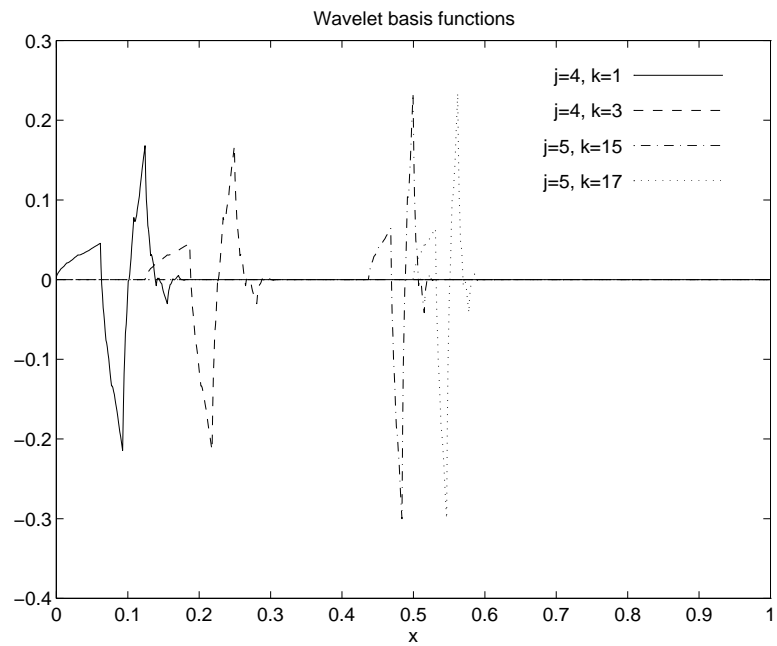


Fig. 2.

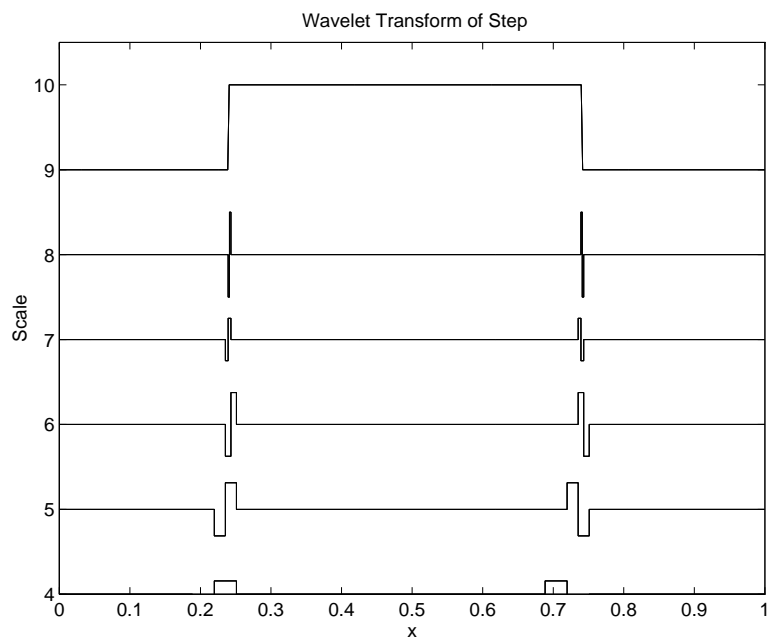


Fig. 3.

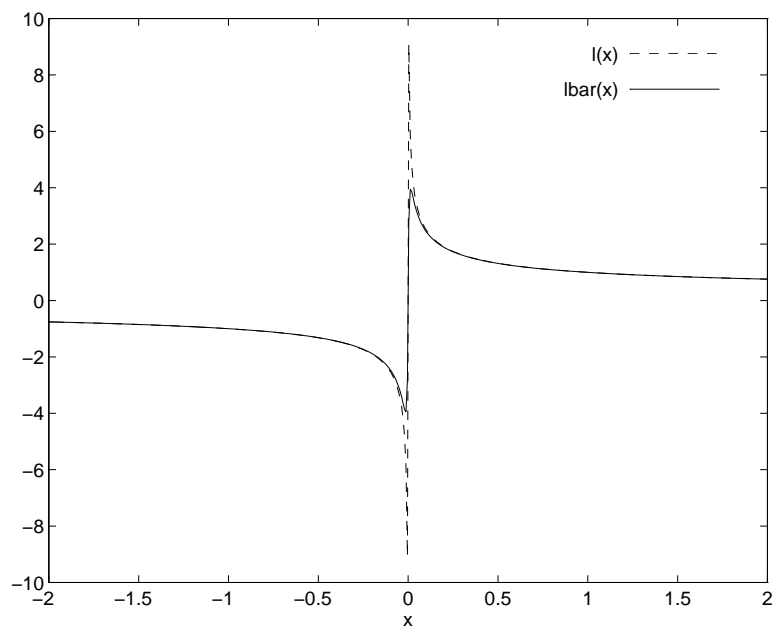
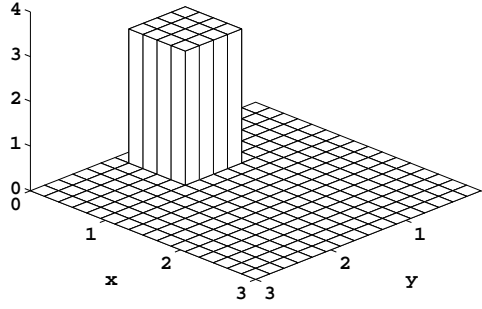
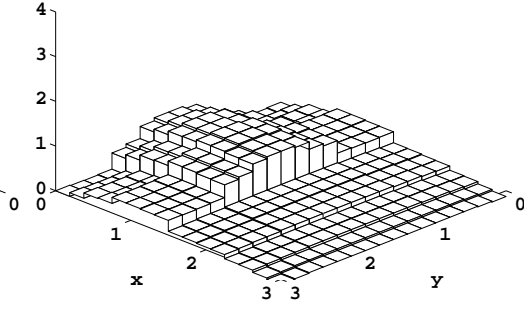


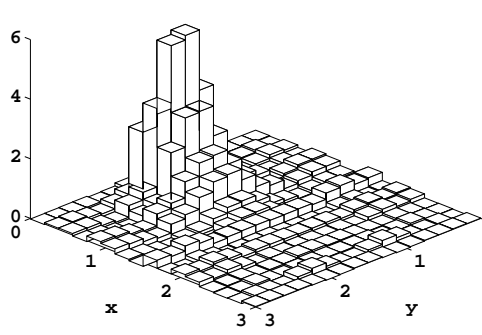
Fig. 4.



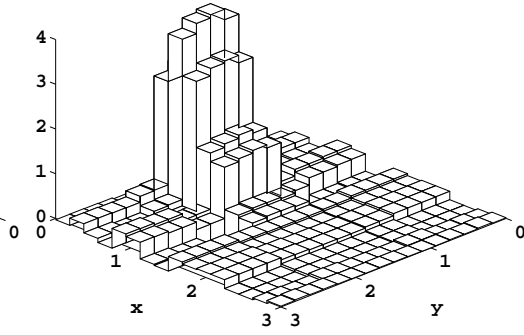
(a) Object Function



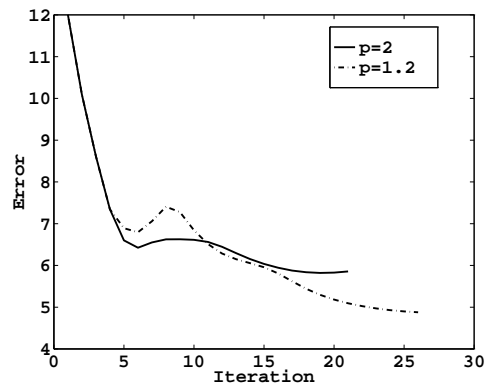
(b) Born reconstruction



(c) 2 norm reconstruction



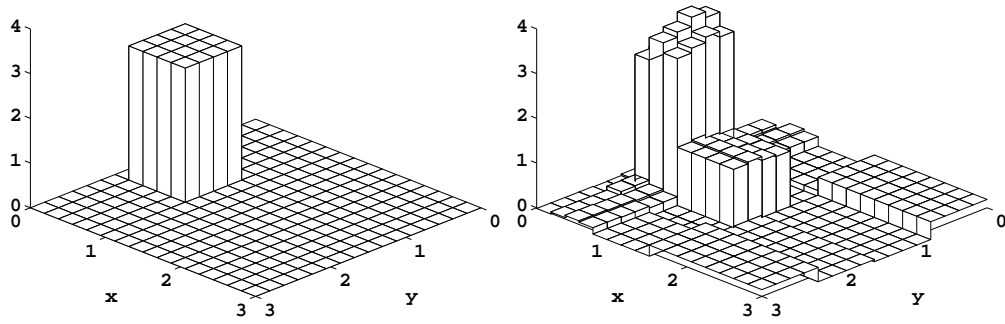
(d)  $p$  norm reconstruction



(e)  $\|\hat{\gamma}_n - \gamma\|_2$

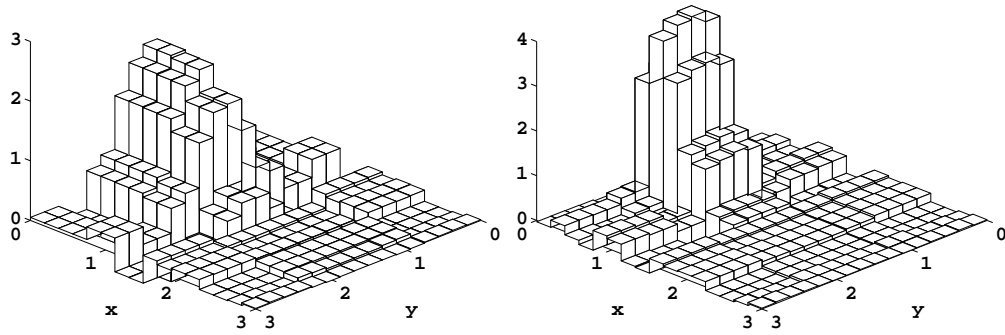
Fig. 5.





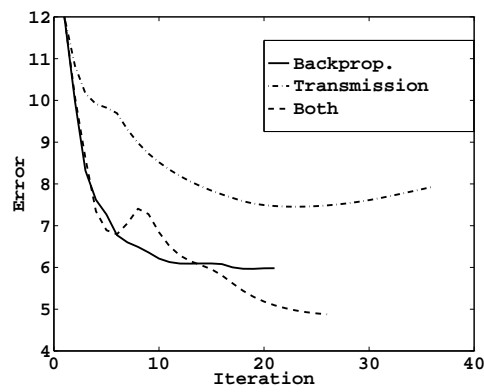
(a) Object Function

(b) Backpropagation reconstruction



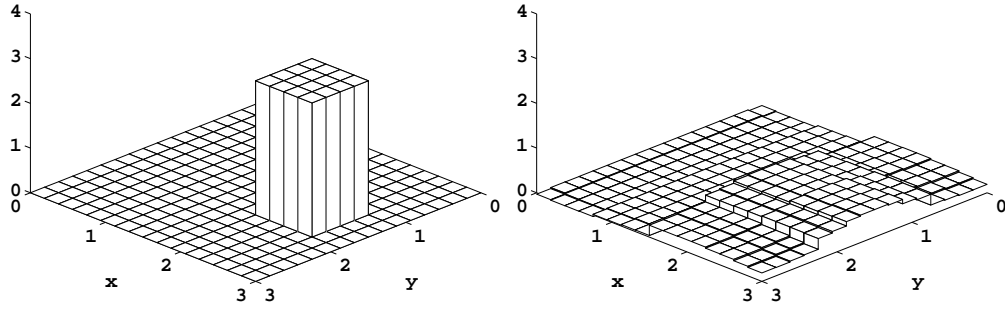
(c) Transmission reconstruction

(d) Combined reconstruction



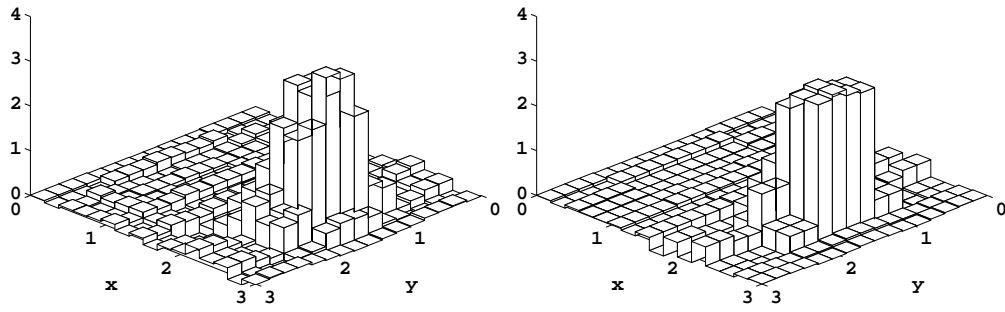
(e)  $\|\hat{\gamma}_n - \gamma\|_2$

Fig. 6.



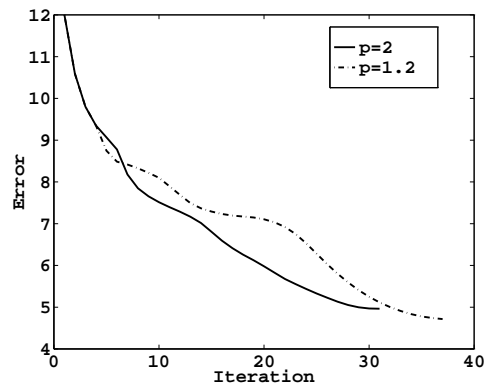
(a) Object Function

(b) Born reconstruction



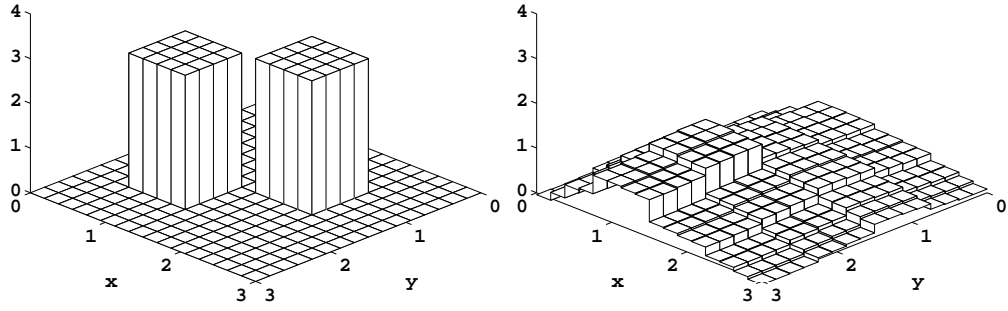
(c) 2 norm reconstruction

(d)  $p$  norm reconstruction



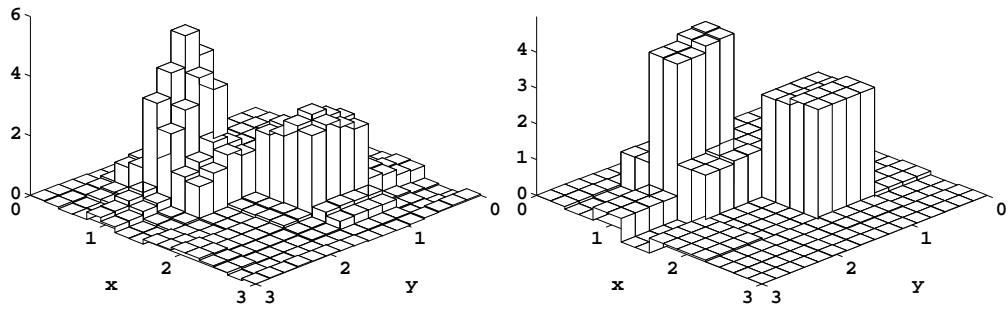
(e)  $\|\hat{\gamma}_n - \gamma\|_2$

Fig. 7.



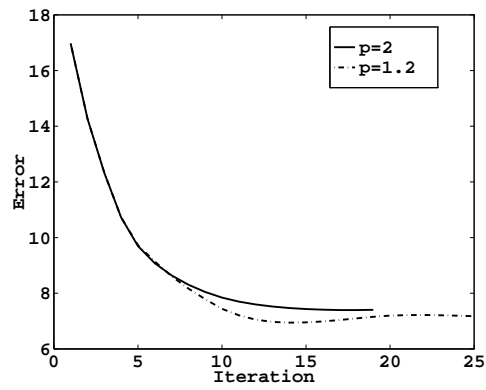
(a) Object Function

(b) Born reconstruction



(c) 2 norm reconstruction

(d)  $p$  norm reconstruction



(e)  $\|\hat{\gamma}_n - \gamma\|_2$

Fig. 8.